Single-shot all-digital approach for measuring the orbital angular momentum spectrum of light

Cite as: APL Photon. 7, 086105 (2022); doi: 10.1063/5.0086536
Submitted: 26 January 2022 • Accepted: 5 July 2022 •
Published Online: 26 August 2022

E. Otte,[1,2,3,a)] V. Bobkova,[1] S. Trinschek,[4] C. Rosales-Guzmán,[5] and C. Denz[1]

AFFILIATIONS

[1] Institute of Applied Physics, University of Muenster, Corrensstr. 2/4, 48149 Muenster, Germany
[2] Geballe Laboratory for Advance Materials, Stanford University, 476 Lomita Mall, Stanford, California 94305, USA
[3] Center for Soft Nanoscience, University of Muenster, Busso-Peus-Str. 10, 48149 Muenster, Germany
[4] Department of Engineering Physics, Münster University of Applied Sciences, Stegerwaldstraße 39, 48565 Steinfurt, Germany
[5] Centro de Investigaciones en Óptica, A.C., 37150 León, Guanajuato, Mexico

[a)] **Author to whom correspondence should be addressed:** eileen.otte@uni-muenster.de and eileen.otte@stanford.edu

ABSTRACT

Light fields carrying orbital angular momentum (OAM) offer a broad variety of applications in which especially an accurate determination of the respective OAM spectrum, i.e., unraveling the content of OAM by its topological charge ℓ, has become a main subject. Even though various techniques have been proposed to measure the OAM spectrum of such modes, many of them fail if optical vortices have to be considered in perturbed or dynamically changing experimental systems. Here, we put forward a novel technique capable of determining the OAM spectrum of light by a single measurement shot, which specifically applies to those fields that have been distorted. Experimentally, our technique only requires to interfere the perturbed light field with a reference field. From the resulting intensity pattern, the accurate OAM spectrum is determined in an all-digital way. We demonstrate our novel approach by numerical simulations and a proof-of-concept experiment employing a model ball lens as an exemplary disturbing object.

I. INTRODUCTION

In 1992, Allen *et al.* reported in their seminal paper that optical vortices with an azimuthally varying phase $\exp(i\ell\varphi)$ carry a well-defined amount of orbital angular momentum (OAM) $\ell\hbar$ per photon.[1] Here, φ is the azimuthal angle of the polar coordinates (r, φ, z), ℓ is an integer number known as the topological charge, which is associated with the number of times the phase wraps around the optical axis, and $\hbar$ is the reduced Planck constant. This discovery ignited a new era of fundamental and applied research, at both the classical and the quantum levels (see, for example, Ref. 2 and references therein). Applications have been proposed in optical micro- and nano-manipulation, optical communications, high-resolution microscopy, and optical metrology, among many others.[3–11] In some of these applications, the OAM of light serves as a path-breaking information carrier. For instance, when a light field interacts with chiral structures of scattering nanoparticles,[11] the OAM of light changes, now carrying information about the chiral nanostructure itself. By OAM analysis, this information can be extracted and nanoscale properties can be unveiled.

Notably, in most applications, an accurate determination of the OAM spectrum, i.e., unraveling the content of OAM by its topological charge ℓ, is crucial, leading to several proposals on how to measure it. Since the early days, many techniques have relied on interferometric approaches, in some of which the unknown field interferes with a plane wave[12,13] or an inverted copy of itself.[14–20] Thereby, the discrete topological charge is extracted from the interference pattern, for example, by counting the number of arms in the spiraling intensity strips pattern. Other techniques employ diffraction phenomena, e.g., by propagating the OAM-carrying beams through an annular aperture[21] or an axicon.[22] Since the number of bright rings in the far- or near-field intensity profile, respectively, is equal to the discrete topological charge of the beam, the OAM spectrum can be identified. In a variant of these approaches, a

triangular aperture can be implemented.[23] In this case, the bright points at any side of the triangular diffraction pattern are directly related to its topological charge—an approach that has been generalized to also determine the radial index in Laguerre–Gaussian modes.[24] Other approaches include phase-shifting digital holography,[25] the weak measurement principle,[26] and the rotational Doppler effect,[27] to name a few. More recently, the use of customized refractive optical elements has led to the development of a device termed the mode sorter, which allows direct measurement of discrete topological charges. Such a device relies on the conversion of OAM modes into modes with a transverse phase gradient. Depending on their topological charge, the modes are focused to different lateral positions.[28] Subsequently, a generalized digital version of this mode sorter was proposed, to not only measure the topological charge but also the radial index of Laguerre–Gaussian modes, termed the Laguerre–Gaussian mode sorter.[29]

Most of the above-mentioned techniques only allow for extracting discrete ℓ values and/or can be successfully applied only to ideal, i.e., undisturbed vortex beams or beams in static experimental configurations. In contrast, an accurate determination of the continuous OAM spectrum under nonideal conditions represents an open challenge, which includes light propagating through a faulty, e.g., astigmatic optical system, under atmospheric turbulence, or when experimental settings change dynamically. This can be the case, for example, in fiber or free-space optical communication with structured light.[9,10,30] Here, one of the "killing" factors is the resulting modal-crosstalk, which leads to a broadening of the OAM spectrum. This crosstalk ultimately reduces the transmission capacity of the optical link.[31] One of the main effects caused by the example of turbulence is the transverse shift of transmitted modes (also known as tip or tilt). Nonetheless, for an optical vortex beam to be accurately detected, its phase singularity (point of undefined phase) has to be centered with respect to the OAM decoding system, e.g., the transverse phase vortex encoded in a decoding hologram.[32] Any misalignment will result in a crosstalk: As OAM beams represent a complete mode set, a misaligned optical beam can be represented as a complex linear combination of different OAM modes.[33] As a consequence, the OAM spectrum significantly and unintentionally broadens. Therefore, many approaches have been proposed to overcome such issues.[34–38] For example in Ref. 34, the authors proposed to use optical modes with less sensitivity for transverse shifts, such as Hermite–Gaussian modes. Alternative approaches suggest to identify the tilt angle and correct for this aberration either by recovering the phase distribution of the tilted OAM mode or by the use of machine learning techniques.[37–39]

Nevertheless, the accurate alignment of a physical electric field of interest to its likewise physical, analog optical decoding system remains a major challenge, especially when disturbances or dynamic changes are involved. The implementation of digitally controllable elements as spatial light modulators (SLMs) or digital mirror devices (DMDs) eases this process; however, they cannot fully solve the problem. They allow for digital, computer-generated decoding holograms, which can be adapted dynamically and enable including, for instance, correcting functions for some disturbances. However, accurate hologram position and correcting functions have to be determined beforehand, but they might change dynamically. Hence, to enable accurate determination of the OAM spectrum of light under nonideal, maybe dynamically varying conditions, we propose to go all-digital.

In this work, we present an all-digital technique aimed at extracting the continuous OAM spectrum of a disturbed light field, with specific applications to those that have suffered from small perturbations due to, for instance, lens aberrations or angular misalignment. We demonstrate this approach through numerical simulations and a proof-of-concept experiment, using a glass ball lens as the perturbing medium. We transform the physical light field of interest into a digital one by established digital holographic phase metrology[40] (DHPM)—the interference of the target optical field with a reference field—and, subsequently, digitally process the recorded interference pattern. This single-shot measurement facilitates the accurate determination of the continuous OAM spectrum by implementing adaptable correction patterns, paving the way to OAM spectrum analysis in dynamic, high-speed systems. For this purpose, we implement tools of singular optics for precise identification of the transverse decoding position in light. Further, we highlight the effect of typical errors occurring in physical decoding systems on the OAM spectrum and present approaches for their correction by our all-digital technique. The proposed all-digital, single-shot approach is particularly beneficial for high-speed investigations, less sensitive to errors such as imperfections of optical systems, and enables the accurate determination of continuous OAM spectra with high precision due to optimized and automated determination of the decoding position and correction of dynamically changing disturbances.

II. DETERMINING THE OAM SPECTRUM OF LIGHT

A. Standard holographic OAM decoding

To holographically decode the OAM spectrum of a scalar light field $E = E_0 \cdot \exp(\mathrm{i}\phi)$, a combination of a phase-only spatial light modulator (SLM) and a Fourier lens ($\mathrm{L}_{\mathcal{F}}$) is typically applied,[32] as illustrated in Fig. 1(a). Thereby, the field E is multiplied by the SLM phase function in the SLM plane (=real space) and the lens creates the far field of the result on a detector, e.g., a camera. This standard decoding approach relies on the inner product of E and each of the OAM-carrying modes $u_\ell = \exp(\mathrm{i}\ell\varphi)$ ($\varphi \in [0, 2\pi]$) in the subspace of interest $\ell = [\ell_{\min}, \ell_{\max}]$. This technique is based on modal decomposition (for more details, see Ref. 32), where we assume that each optical field can be expressed as a linear combination of basis functions from an orthogonal set of spatial modes,[32]

$$u(\vec{r}) = \sum_{\ell=1}^{\infty} c_\ell u_\ell(\vec{r}), \tag{1}$$

with spatial coordinate $\vec{r}$ and complex coefficient $c_\ell = \rho_\ell \exp(\mathrm{i}\phi_\ell)$, its amplitude ρ_ℓ and intermodal phase $\Delta\phi_\ell = \phi_\ell - \phi_0$. By displaying u_ℓ^* as a phase-only function (hologram), that is, $\arg(u_\ell^*) = -\ell\varphi$ on the SLM, the product $\rho_\ell^2 = |\langle u_\ell | E \rangle|^2$ is shaped. In this case, the on-axis intensity in the Fourier plane of the SLM, i.e., on the detector, is proportional to the power content of the OAM mode of topological charge ℓ. By measuring the power content per ℓ of interest, displaying the according function $\arg(u_\ell^*)$ on the SLM, the OAM spectrum of E is determined.

Note that one can choose to display multiple decoding holograms at a time by, e.g., angular/spatial multiplexing[41–43] in order to

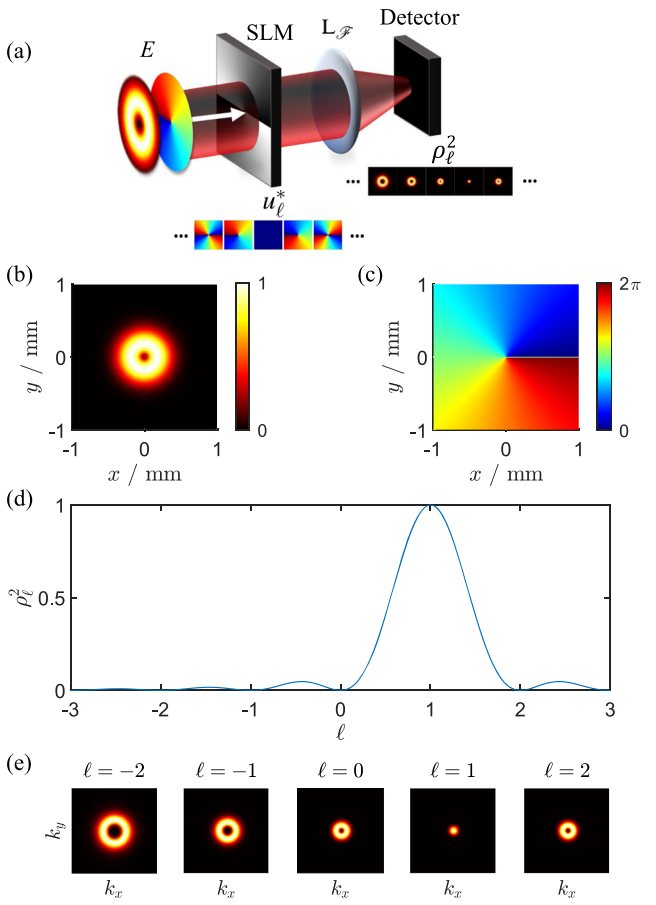

FIG. 1. Holographic OAM spectrum analysis of a light field under ideal conditions. (a) The typical experimental scheme: The electric field E of interest is modulated by the hologram of u_ℓ^*, encoded onto a phase-only spatial light modulator (SLM), and is subsequently 2D Fourier transformed onto a detector by a Fourier lens ($L_{\mathscr{F}}$), forming the product $\rho_\ell^2 = |\langle u_\ell | E \rangle|^2$. The amplitude E_0 and the phase ϕ of the exemplary scalar field E, i.e., the Laguerre–Gaussian (LG) field with $w_0 = 0.25$ mm, $\ell = 1$, and $p = 0$ are shown in (b) and (c), respectively. (d) The respective normalized OAM spectrum is extracted from (e) the intensity $\rho_\ell^2 = |\langle u_\ell | E \rangle|^2$ in Fourier space (examples for $\ell = [-2, 2] \in \mathbb{N}$).

speed up the measuring process. In this case, each hologram u_ℓ^* is assigned to a selected spatial carrier frequency by adding a blazed grating such that ρ_ℓ^2 is found at different transverse positions in the Fourier space. Thereby, the system has to be calibrated with respect to the diffraction efficiency per grating. Further, the number of simultaneously displayed holograms is limited by, for instance, the resolution of the SLM.

We illustrate this standard approach (without multiplexing) in Fig. 1 (simulation) for decoding the OAM spectrum of a helical Laguerre–Gaussian (LG) light field described by a complex amplitude,[44–46]

$$\mathrm{LG}_{p,\ell}(r, \varphi, z) = A_{p,\ell}(r, z) \cdot \mathrm{e}^{\mathrm{i}\frac{kr^2}{2R(z)}} \cdot \mathrm{e}^{\mathrm{i}\phi_{p,\ell}^G(z)} \cdot \mathrm{e}^{\mathrm{i}\ell\varphi}, \tag{2}$$

$$A_{p,\ell}(r, z) = \sqrt{\frac{2p!}{\pi(|\ell| + p)!}} \cdot \frac{1}{w(z)} \cdot \mathrm{e}^{-\frac{r^2}{w^2(z)}} \times \left(\frac{r\sqrt{2}}{w(z)}\right)^{|\ell|} \cdot \mathrm{L}_p^{|\ell|}\left(\frac{2r^2}{w^2(z)}\right), \tag{3}$$

$$\phi_{p,\ell}^G(z) = (2p + |\ell| + 1)\phi_{0,0}^G(z), \tag{4}$$

where k is the wave number, $R(z)$ the wave front curvature, $w(z)$ the beam radius, $w_0 = w(0)$ the beam waist, $p \in \mathbb{N}_0$ the radial mode index, $L_n^\ell(\cdot)$ the eponymous Laguerre polynomial,[47] $\phi_{n,\ell}^G$ the Gouy phase shift of LG light fields, and $\phi_{0,0}^G$ the Gouy phase shift of fundamental Gaussian light field. The phase vortex structure $\exp(\mathrm{i}\ell\varphi)$ is related to a twisted wave front upon propagation and causes the formation of a point of undefined phase, i.e., a phase singularity on the propagation axis of LG fields. The optical decoding by the system of SLM, Fourier lens, and detector is simulated by the two-dimensional (2D) Fourier transform ($\mathscr{F}$) of the product of the electric field and the phase function of the SLM hologram, i.e., $\mathscr{F}[E \cdot \exp(-\mathrm{i}\ell\varphi)]$.

Note that ℓ is also considered as the singularity index of the embedded phase singularity ($\ell_{\mathrm{sing}} = \oint \mathrm{d}\varphi/2\pi \in \mathbb{Z}$) and, for those, represents a conserved quantity.[48,49] However, ℓ (integer and fractional) is also established as a measure for OAM of vortex beams and is used as such in the context of this work.

The exemplary scalar light field has a topological charge $\ell = 1$, radial index $p = 0$, and beam waist $w_0 = 0.25$ mm. Its ring-shaped intensity and vortex phase are presented in Figs. 1(b) and 1(c), respectively. When this light field passes the analysis system of SLM and Fourier lens, in Fourier space, we observe intensity structures as illustrated in Fig. 1(e) for integer $\ell = [-2, 2]$. Considering the respective on-axis intensities as the power content per OAM mode, we can determine the OAM content or spectrum, as presented in Fig. 1(d). Note that, here and in the following, we also consider fractional OAM values with $\ell = [-3, 3], \in \mathbb{R}$, resulting in continuous OAM spectra, which are of specific interest for applications in optical sensing based on OAM,[3,4] in particular in nanoscale systems[11] and/or if minimal changes in OAM content might be of interest. As expected, a clear, absolute maximum is observed for $\ell = 1$, reflecting the chosen topological charge of the exemplary LG field. While, as expected, for integer values with $\ell \neq 1$, minima ($= 0$) are found, OAM of fractional ℓ values reveals nonzero contributions to the total spectrum. This is due to the fact that modes of fractional ℓ can again be represented by the complete mode set of integer OAM fields and, therefore, also contain contributions of OAM modes of charge $\ell = 1$.

Even though this measurement procedure is well established, it still presents some challenges to the general user. One of these challenges is the appropriate transverse positioning of the decoding hologram in relation to the optical axis of the light field or, more precisely, to the center of the embedded optical vortex, which represents the carrier of OAM information. In Fig. 2, we illustrate the effect of misaligning hologram and optical vortex when analyzing the OAM spectrum of light. Again, we use the $\mathrm{LG}_{0,1}$ field as illustrative example. We assume a transverse mismatch between the LG field and the hologram by changing the x-distance between their centers. Note that the position of the hologram is shifted by Δx in the x-direction,

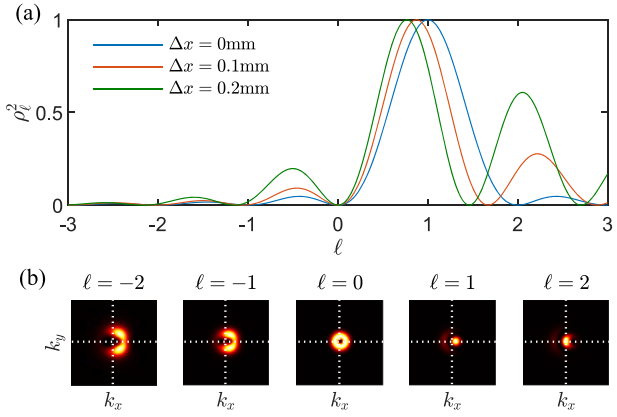

FIG. 2. Effect of misalignment between light field and decoding phase field. The center of the decoding phase is shifted with respect to the light field center in the x-direction by a small distance Δx. (a) The respective calculated OAM spectrum of the LG field shown in Fig. 1. The intensity of the Fourier transforms of the electric field multiplied by the phase field are exemplified in (b) for the misalignment $\Delta x = 0.2$ mm ($= 0.8 w_0$).

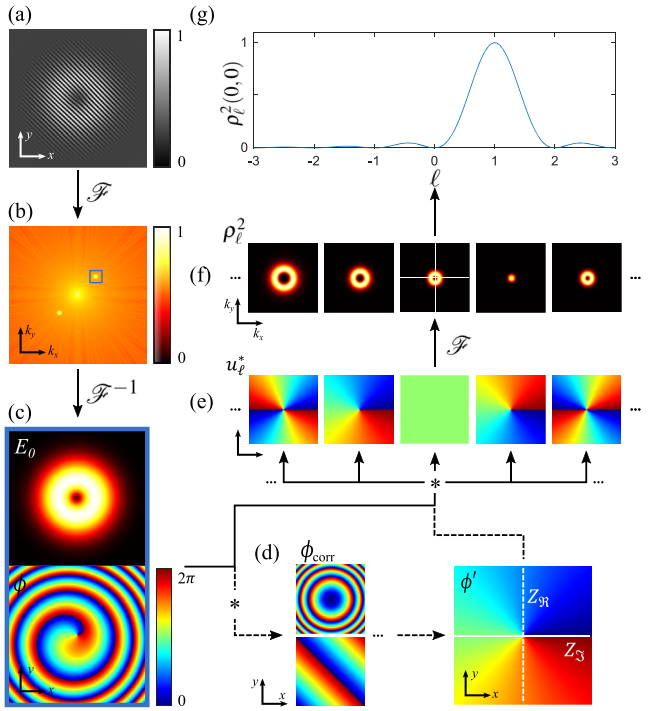

FIG. 3. Concept of single-shot, all-digital OAM spectrum analysis. (a) Off-axis interference pattern of the light field of interest E and reference plane wave (in experiment, measured on a camera), which is Fourier transformed ($\mathscr{F}$), giving the pattern in (b) (logarithmic representation). By selection of the first diffraction order (blue box) and inverse Fourier transform ($\mathscr{F}^{-1}$), the (c) amplitude E_0 and phase ϕ of the complex electric field E can be extracted. (d) Correcting phase patterns ϕ_{corr} can be applied to optimize the final OAM spectrum results ($\phi \to \phi' = \phi + \phi_{corr}$). Subsequently, the measured $E = E_0 \cdot \exp(i\phi)$ [or $E' = E \cdot \exp(i\phi_{corr})$] is (e) multiplied by the digital holograms u_ℓ^* (for integer as well as fractional ℓ), which are adjusted according to the singularity position in (c) ϕ [or (d) ϕ'], found by zero-lines $Z_{\Re,\Im}$ as exemplified in (d) (right). (f) Fourier transform is used to determine ρ_ℓ^2 on the optical axis $(k_x, k_y) = (0,0)$, representing the contribution per OAM mode and giving (g) the OAM spectrum.

while the light field stays centered at $(x, y) = (0, 0)$, assuming that, in the corresponding experiment, the field and Fourier lens are well-adjusted in the optical system. Figure 2(a) reveals an increasing shift (in negative ℓ direction) in the OAM spectrum for increasing Δx (orange, green), with its distribution deviating from the ideal curve (blue). The respective change of the intensity distribution in Fourier space ρ_l^2 (on the detector) is exemplified for $\Delta x = 0.2$ mm in Fig. 2(b). For a mismatch of the holograms and the light field center, the main contribution in OAM spectrum is no longer located at $\ell = 1$, but it is shifted to fractional values $\ell < 1$ and significant contributions at integer values $\neq 1$ appear (e.g., $\ell = 2$). Note that this shifted spectrum represents the correct OAM for the chosen point of reference, i.e., the central position of the shifted hologram. However, we are interested in the overall OAM carried by the beam in its propagation direction, i.e., the point of reference has to be located on the optical axis of the beam.

Deviations from the accurate OAM spectrum, appearing for an incorrect point of reference, may become critical and cause incorrect results when implementing optical spectrum analysis in applications, such as information transfer and encoding[50,51] or the study of chiral media/structures.[11] Optical systems can generally be optimized such that the light field and the hologram center are matched as closely as possible. However, an exact match is hard or even impossible when the light field is moving in the transverse plane, e.g., as a result of propagation through a refracting, maybe, dynamic medium. The identification of the phase vortex center of the field is further complicated by the fact that the center of OAM-carrying light fields is, in general, dark with low to zero intensity. Tackling these issues, in the following, we propose an alternative all-digital approach to optimize holographic OAM spectrum analysis.

B. Single-shot, all-digital OAM spectrum analysis

The proposed all-digital OAM spectrum analysis is sketched in Fig. 3 (simulations), exemplified for $E = \mathrm{LG}_{0,1}$. For this approach, we first apply the established digital holographic phase metrology (DHPM; for details, see Refs. 40, 52, and 53) to extract the amplitude and the phase of the light field E of interest and, simultaneously, digitalize it. Thereby, E (real space) is interfered off-axis with a plane wave of the same polarization. In the experiment, this plane wave is approximated by an expanded, collimated Gaussian laser beam. The formed transverse interference pattern [Fig. 3(a)] is recorded on a detector (camera) in real space—this pattern is all what is needed to subsequently extract the OAM spectrum digitally. In the next step, the interference pattern is Fourier transformed ($\mathscr{F}$), giving a complex 2D field [intensity in Fig. 3(b)]. In this field, we identify and crop [see blue box in (b)] the contribution of E, located at nonzero spatial frequencies in k-space (Fourier space) with the location depending on the interference angle. The inverse Fourier transform ($\mathscr{F}^{-1}$) of the cropped complex field gives the measured electric field E with amplitude E_0 and phase ϕ [Fig. 3(c)]. Note that measured phase values are only to be considered at positions where E

is not approximately zero. Otherwise, random phase values (speckles) contribute to the later OAM spectrum. To do so in experiment, we derive a binary 2D mask from the measured amplitude, deleting all outer electric field information (i.e., the dark center of a donut beam will be kept) where the intensity $|E_0(x,y)|^2$ is smaller than 3% of its maximum.

In order to extract the OAM spectrum of the light field, we perform the multiplication of $E = E_0 \cdot \exp(\mathrm{i}\phi)$ with the hologram functions u_ℓ^* per ℓ [Fig. 3(e)], Fourier transform the product [Fig. 3(f)], and determine the on-axis intensity in Fourier space [white cross in (f)] being proportional to the OAM mode contribution [resulting spectrum in Fig. 3(g)]. To avoid deviations due to misalignment of E and the hologram, we center the hologram according to the position of the optical phase singularity in E [or $E' = E \cdot \exp(\mathrm{i}\phi_{\mathrm{corr}})$, see details below], which is naturally included for most OAM-carrying light fields. For this purpose, we use zero-lines[54–56] of the real ($Z_{\Re}$) and imaginary ($Z_{\Im}$) part of E (E') to identify an embedded phase singularity as zero-line intersection. The implementation of zero-lines has the advantage that the singularity identification can be performed all-digitally without the requirement of alternative extended algorithms searching for a 2D phase vortex structures by comparison of neighboring pixels. Zero-lines are exemplified for the corrected phase pattern (see outline below) by white dashed and solid line in Fig. 3(d), ϕ'. If E carries OAM of $\ell\hbar$/photon with $|\ell| \geq 2$, as in the case of higher-charged LG beams, a nongeneric higher-order phase singularity is expected in ϕ, which, in experiment or in combination with other spatial modes, splits into multiple closely neighboring, generic first-order ($|\ell| = 1$) phase singularities[54,56] due to perturbations. In this case, the center of the hologram is chosen to be the center between all identified first-order singularities. An example for this approach is depicted in the supplementary material, Fig. 1. It presents the OAM decoding results (simulations) for a 50/50 combination of a Gaussian beam ($\mathrm{LG}_{0,0}$) and a higher-order $\mathrm{LG}_{0,3}$ beam when positioning the holograms at the geometrical center of split singularities. Note that one can also choose to crop the field of view of measured E such that the found singularity or a circle of split singularities is centered and, subsequently, place the hologram centered.

To successfully employ the singularity position(s) for adjusting the hologram, we have to ensure that the measured interference pattern [Fig. 3(a)] is of high contrast and the area of low intensity around singularities (central part of the ring-shaped intensity) is appropriately resolved. Optimally, the intensity in the central area only becomes zero at the position of the singularity itself. In this case, the singularity position is clearly defined. With decreasing resolution of the central area of low intensity, the precision in determining the singularity position(s) and, subsequently, the OAM spectrum, decreases as well.

The described procedure also allows for additional optimization steps [Fig. 3(d)] prior to OAM spectrum extraction, which can be of benefit depending on the perturbations the light field of interest experiences and the therefrom resulting phase distribution ϕ. We exemplify this option in the following by analyzing an $\mathrm{LG}_{0,1}$ field refracted by a ball lens—first numerically and, in Sec. V, experimentally. Since the angular momentum of light is a conserved quantity, the OAM content of the light field is expected to be unaffected by the refraction by a ball lens. This allows us to suggest and investigate approaches to correct for typical errors that can disturb the resulting OAM spectrum. Note that, even when including possible correction steps, the outlined measurement procedure is unchanged and still requires only a single-shot recording of the interference pattern.

III. THE EFFECT OF WAVE FRONT CURVATURES

A wave front curvature of a light field appearing in combination with embedded phase vortices can disturb the outcome of an OAM spectrum analysis: Additional curvatures result in a change in the Fourier space distribution of the light field E and, therefore, easily cause errors when extracting the power content per OAM mode. As outlined above, the Fourier transform represents the focusing of the field multiplied by the hologram through a lens. Thus, wave front curvatures, similar to lens errors, can cause a transverse and also longitudinal shift of the lens' focus position in Fourier space, thereby perturbing the read-out of the power content. However, such effects can also be negligible depending on the symmetry of the wave front curvature. We illustrate this by the example of the $\mathrm{LG}_{0,1}$ beam passing through a ball lens, adding (among other features) spherical wave fronts to the light field.

Propagating through a ball lens in air, a light field is strongly refracted, experiencing aberrated focusing.[57] For the $\mathrm{LG}_{0,1}$ beam passing through a glass ball lens of 2 mm diameter (refractive index $n = 1.458$), the resulting light field distribution is illustrated in Figs. 4(a) and 4(b) (simulations). The beam waist of the LG light field is assumed to be at the front surface of the ball lens with $w_0 = 0.25$ mm. Simulations are performed by the vectorial ray-based diffraction integral (VRBDI) method introduced by Andreas *et al.*[58,59] (for more detailed information, see Ref. 57 where the scheme was applied in a similar setup). We show (a) the three-dimensional (3D) evolution of intensity and (b) the transverse intensity and phase distribution in three selected (x,y)-planes. The spherical wave front before and behind the focal point of the ball lens [see (a)] will cause the phase structure of E to include not only a phase vortex but also an additional phase curvature. Due to aberrations, before the focal point of the ball lens [(b), $z = 1500\ \mu$m], we observe multiple transverse intensity rings and, accordingly, phase jumps in the spiraling phase structure of ϕ. Behind the focal point [(b), $z = \{1600, 1650\}\ \mu$m], a blurred intensity ring is found in the transverse plane, diverging upon propagation in the $+z$-direction. Here, the transverse phase structure only contains a spiral, formed by lines of equal phase value, and no phase jumps, corresponding to the combination of phase vortex and spherical wave front.

Figure 4(c) shows the OAM spectrum of the light field (simulations), refracted by the ball lens, for different z-positions in comparison to the spectrum of the input $\mathrm{LG}_{0,1}$ field (at its beam waist). Even though the phase structure of the refracted field is deviating from the typical, ideal phase vortex as carried by the exemplary $\mathrm{LG}_{0,1}$ field, the OAM spectrum is almost the same. A cylindrical symmetric spherical wave front is responsible for a phase distribution similar to the one corresponding to an optical lens and, therefore, causes the defocusing or focusing of light in its far field, namely, in Fourier space. Thus, when decoding the OAM spectrum by multiplication with the hologram function and subsequent Fourier transform, spherical wave fronts do not affect the relative on-axis intensity observed for different u_ℓ^*. Due to their cylindrical symmetry, the multiple transverse, centered rings in phase and

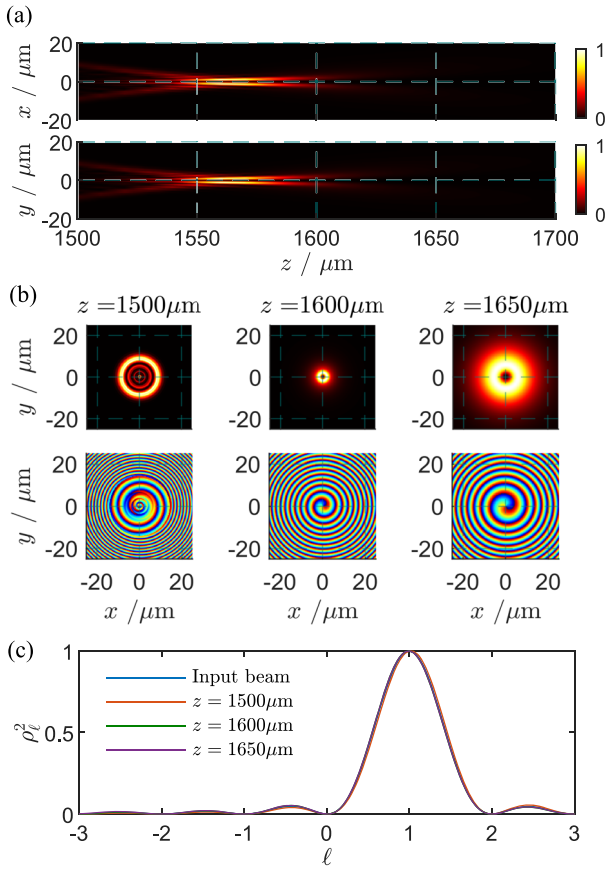

FIG. 4. Simulated light field of the $LG_{0,1}$ beam after passing centered through a ball lens. (a) *x*-*z* and *y*-*z* cuts of $|E|^2$ normalized to the maximum intensity in the plane; *z* values are measured from the center of the ball lens. For three *z*-positions, (b) the intensity (top) and the phase (bottom) are shown in transverse planes. The respective calculated OAM spectra are shown in (c) together with the OAM spectrum of the input light field for comparison. All spectra are normalized to their respective maximum value.

intensity (before the focus of the ball lens) do not affect the on-axis intensity in Fourier space and, hence, the spectrum neither.

In contrast, if a wave front curvature that corresponds to more complex lens errors has to be considered, the spectrum can deviate more significantly from the ideal one. A typical example is that of wave front curvatures with elliptical symmetry, occurring frequently due to, for instance, astigmatic lenses, nonideal fibers, non-flat SLM surfaces, or other optical components in the beam path. In comparison to the ball lens example, we now assume the $LG_{0,1}$ light field to be focused by a thick glass lens of spheroid shape (cf. Ref. 57), with its half axis being R_y = 0.94 mm in the *y*-direction and $R_{x,z}$ = 1.06 mm in the *x*-/*z*-direction. In this case, two focal planes are found due to astigmatism.[57] Figure 5(a) shows the transverse intensity and phase distribution at three different *z*-positions, clearly revealing the elliptical deformation of the originally cylindrical symmetric LG input field. The extracted OAM spectrum at z = 1650 μm (behind both focal planes) is shown in Fig. 5(b) (orange) in comparison to the spectrum of the input field (blue).

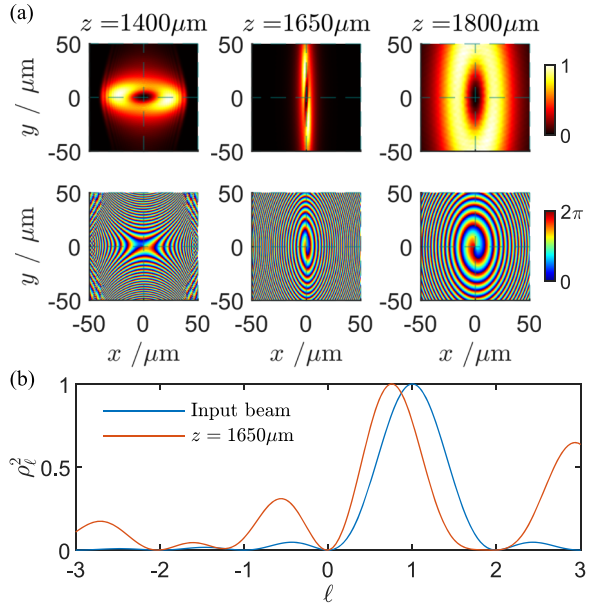

FIG. 5. Simulated light field of the LG input field after passing centered through a spheroid lens with half axis $R_x = R_z$ = 1.04 mm and R_y = 0.96 mm (cf. Ref. 57). (a) Transverse cuts of the intensity (top) and the phase (bottom) at three *z*-positions. (b) Calculated OAM spectrum (normalized; orange) behind both focal planes (tangential and sagittal plane) of the lens at z = 1650 μm in comparison with the normalized OAM spectrum of the input LG light field (blue).

Obviously, the spectrum deviates from the ideal spectrum, showing significant contributions at integer $\ell \neq 1$ values. These contributions should not be found since, for a light field only interacting with such a glass object, OAM should be conserved. The reason for this error in OAM spectrum analysis is the effect of the elliptical wave front in Fourier space. Under Fourier transform, an elliptical wave front acts like an astigmatic lens (not to be confused with the spheroid lens we applied for creating the field under investigation). When holographically extracting the OAM spectrum, this effect can be considered as applying a nonideal Fourier lens to the OAM-carrying part of the field. In this case, the horizontal and vertical distributions of the light field are focused and, thus, decoded (=ideally Fourier transformed) in different *z*-planes (sagittal and tangential plane). Hence, when selecting an observation plane, it does not represent the required Fourier transform and the extracted OAM spectrum is incorrect.

The proposed experimental all-digital OAM spectrum analysis provides the opportunity to correct for these or similar errors due to wave front curvatures. After performing DHPM, the wave front curvature can be neutralized by multiplying the measured electric field distribution by a 2D correction pattern $[E \cdot \exp(i\phi_{corr}) = E']$; see Fig. 3(d)]—for instance, an inverse spherical lens. This will be exemplified in Sec. V. For a precise determination of the required correction, we unwrap the measured phase distribution via a robust unwrapping algorithm, which is described in Ref. 60. This algorithm allows transforming the 2π-folded, 2D phase map into a continuous one, going beyond 2π values. In this map, the azimuthal phase gradient corresponding to a phase vortex is minor in comparison

to the one corresponding to a curved wave front. Hence, we fit this continuous map by a 3D ellipsoid function and create the required phase correction from this fit. As an alternative approach, the correction can be estimated by determining the phase gradient pointing away from the phase singularity. This gradient can be used to create an elliptical lens-like phase correction. The position of the singularity in E is determined from zero-line intersection and does not necessarily match the center of the spiral observed in ϕ, formed by lines of equal phase value [Fig. 3(c), ϕ]. This effect is due to additional phase factors, namely, a phase ramp. This typical distortion can be caused by an angular misalignment of the normal vectors on the decoding plane and (x, y)-plane of the light field of interest and will be described in more detail in Sec. IV. Note that before determining and applying the correction for the curved wave front, phase ramps should be considered, since this moves the spiral in ϕ back to surrounding the singularity. If it has been estimated, ϕ_{corr} for the curved wave front should be positioned according to the singularity position.

IV. ANGULAR MISALIGNMENT OF LIGHT FIELD AND DECODING PLANE

When analyzing the OAM spectrum of a light field, the plane of observation does not necessarily match the propagation direction of the field, i.e., the normal vector on the observation (=decoding) plane and wave vector $\vec{k}$ of light field propagation are not parallel to each other. Similar to a transverse mismatch between the decoding hologram and the beam center (see Sec. II A), this angular deviation is equal to an incorrect point of reference for the determination of OAM spectrum. This can easily occur, for instance, when the light field is meeting the SLM, used for holographic OAM decoding, under an angle—SLMs are often set up like this to allow for independent incoming and reflected beam paths. Further, when OAM-carrying fields are used for metrology, they interact with media, which might change their propagation direction. To exemplify this case, we simulate the $LG_{0,1}$ field propagating through the ball lens with its propagation axis parallelly shifted by $\Delta x = 0.1$ mm. Hence, the LG field does not meet the ball lens center. The resulting 3D structured light field E behind the ball lens is depicted in Figs. 6(a) and 6(b). The (a) evolution of intensity upon propagation as well as (b) the selected z-slices reveal aberrational effects with multiple transverse intensity rings before the focal plane ($z = 1450$ μm) and smearing of intensity rings behind the focus ($z = \{1600, 1650\}$ μm). The asymmetry in the light field distribution depicts the tilting of $\vec{k}$ in the x-direction, also visible in (a). The tilting becomes particularly visible when observing the dark center (phase singularities) of the ring-like intensity structures in the transverse planes, which are clearly shifted off-axis.

If the propagation direction of light ($\vec{k}$) is not perpendicular to the observation plane, one will observe a 2D phase ramp in the transverse phase ϕ structure of E. For the presented example in Fig. 6, this phase ramp affects the observed transverse phase structure shown in (b), clearly deviating from the case in which the light field passes the ball lens centered [cf. Fig. 4(b)]. In this case, we observe not only the effect of aberration and wave front curvatures but additionally asymmetric deformation and the effect of tilted light field propagation.

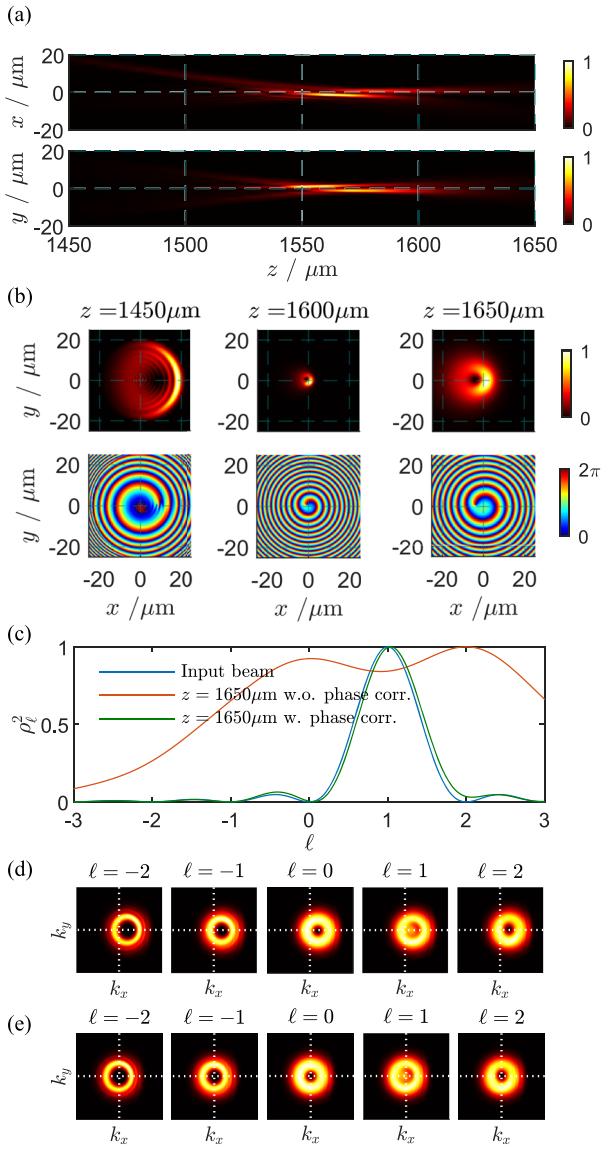

FIG. 6. Simulated light field of the $LG_{0,1}$ beam after passing through a ball lens with an offset of $\Delta x = 0.1$ mm between lens center and beam axis. (a) x-z and y-z cuts of $|E|^2$ normalized to the maximum intensity in the respective plane. For three z−positions, (b) the intensity (top) and the phase (bottom) of E are shown in transverse planes. Normalized OAM spectra calculated at $z = 1650$ μm with and without correction of the phase ramp and the OAM spectrum of the input light field for comparison are presented in (c). The intensity of the Fourier transforms of the electric field multiplied by the phase function $\exp(i\ell\varphi)$ are shown without phase ramp correction in (d) and with phase ramp correction in (e). The phase ramp correction corresponds to a shift in Fourier space.

Under Fourier transform, a phase ramp (angular mismatch) is identified as a transverse position shift of the far field distribution. Hence, when applying the digital hologram u_ℓ^* and Fourier transforming this multiplication to extract the OAM spectrum of E, the

respective distribution will not show the power content per OAM mode at $(k_x, k_y) = (0, 0)$, but shifted. In Fig. 6(d), the Fourier space distribution is shown for the ball lens example, revealing the transverse position shift ($z = 1650\ \mu$m; no wave front corrections applied; holograms matched to singularity position). This shift results in an incorrect OAM spectrum, as illustrated in Fig. 6(c), red curve. In experiments, if the expected OAM spectrum is known, often the read-out position for the power content is adapted to the maximum of a Gaussian-like distribution [cf. Fig. 1(d), for $\ell = 1$]. However, prior knowledge is not always given or the complex light field structure, as in the case of the field being refracted by a ball lens, does not give a Gaussian-like distribution in Fourier space [see Fig. 6(d)]. In addition, especially in dynamic experiments (e.g., analyzing fluid dynamics[4]), the phase ramp and, thus, transverse position shift in Fourier space can change in time. Our all-digital approach allows for easily correcting errors appearing due to angular mismatch of observation plane and beam path.

As outlined above, corrections are typically applied to E after the single-shot measurement of E_0 and ϕ (DHPM)—we apply correcting phase structures ϕ_{corr} to ϕ. In the case of the tilted beam path, one has to correct for the respective phase ramp, such that the observation plane is matched to the propagation direction of the light field. Showing the effect of this correction, we determine and apply the phase ramp for the ball lens simulation in Fig. 6. The correction is given by $\phi_{corr} = \alpha k x$ ($k = 2\pi/\lambda$) with angle α representing the angular mismatch of light field propagation direction and the normal vector on the observation plane. This angle is $\alpha = -0.06$ rad, calculated from the singularity positions in ϕ for $z = 1600$ and $1800\ \mu$m. When applying ϕ_{corr} to E prior to OAM decoding, the Fourier space distribution is centered around $(k_x, k_y) = (0, 0)$, as exemplified in Fig. 6(e). Extracting the power content per OAM mode as $\rho_\ell^2(0, 0)$ gives an OAM spectrum (green) almost perfectly matching the spectrum of the input LG field (blue curve).

In experiment, performing a single-shot measurement at only one z-position of the light field, the determination of ϕ_{corr} and correspondingly the extraction of α have to be performed differently. In this case, we take advantage of the Fourier space distributions of the recorded interference pattern [Fig. 3(b)]. First, we calibrate our measurement system by interfering the reference field (plane wave) with our signal field, which is later our light field of interest. The signal field can be a Gaussian or a LG light field (of known integer ℓ), not passing any object that is, for instance, supposed to be investigated by the signal field or whose effect on the signal field is of interest—in the example of this work, the ball lens represents the object. An interference pattern is recorded and the corresponding position $\vec{k}_{ref} = (k_{x,ref}, k_{y,ref})^T$ of the signal field in Fourier space is determined. Any deviation from this position $\vec{k}_{ref}$ when subsequently measuring the field E of interest (e.g., the field behind the ball lens) by DHPM will result in a phase ramp in ϕ. A comparison of the k-space position of E ($\vec{k}_E$), which could vary in time in a dynamic system, and $\vec{k}_{ref}$ enables the calculation of the corresponding phase ramp and, thus, its correction before extracting the OAM spectrum. Note that this approach additionally corrects for any kind of misidentification of $\vec{k}_E$ when performing DHPM of E. Conversely, considerate selection of $\vec{k}_E$ can be used to avoid phase ramps in E.

V. EXPERIMENTAL EXAMPLE OF A SINGLE-SHOT, ALL-DIGITAL OAM SPECTRUM ANALYSIS

To experimentally demonstrate the described single-shot, all-digital approach for decoding an OAM spectrum, we analyze a light field refracted by a ball lens of 2 mm diameter. The experimental setup to create the refracted light field E and to obtain the respective interference pattern with a reference wave is shown in Fig. 7(a). Using a q-plate of charge $q = 1/2$[61] (Thorlabs, WPV10L-532),

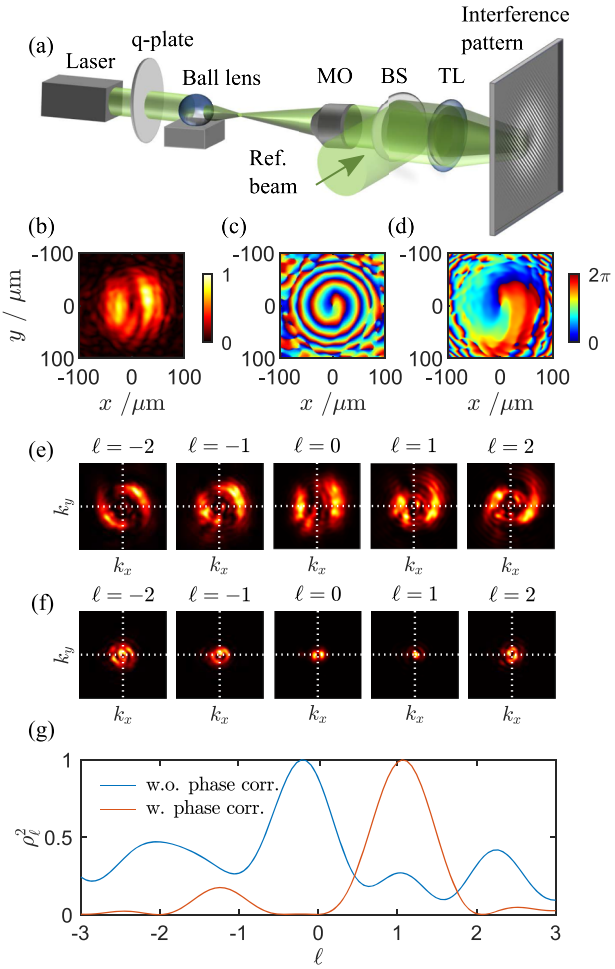

FIG. 7. An example of experimental OAM spectrum analysis of an $LG_{0,1}$ field, refracted by a ball lens. (a) Experimental system consisting of laser ($\lambda = 532$ nm), q-plate ($q = 1/2$; Thorlabs, WPV10L-532), ball lens (refractive index $n = 1.458$, 2 mm diameter), 20× microscope objective (MO, numerical aperture NA = 0.4), 50/50 beam splitter (BS) used to include the reference (Ref.) field, tube lens (TL, focal distance $f = 200$ mm), and detector recording the interference pattern. DHPM allows measuring (b) the amplitude E_0 and (c) phase ϕ of the refracted field E. (d) Measured phase ϕ can be corrected by ϕ_{corr} corresponding to a spherical wave front; $\phi + \phi_{corr}$ is shown. The intensity in Fourier space after multiplication of E (E') with hologram functions u_ℓ^* is shown (e) without and (f) with correction applied for exemplary ℓ. The on-axis intensity values $\rho_\ell^2(0, 0)$ give (g) the respective OAM spectra (normalized).

a Gaussian laser beam (circular polarization, $\lambda = 532$ nm) is transformed into a hypergeometric Gaussian field[62] with its beam waist positioned at the ball lens center. This light field can be approximated as a Laguerre–Gaussian field of topological charge $\ell = 1$ and $p = 0$. The $LG_{0,1}$ beam is focused by the ball lens and the field E at $z \approx 1850\ \mu$m is imaged by a 20× microscope objective (MO; numerical aperture NA = 0.4) and a tube lens (TL, focal length $f = 200$ mm) onto a camera. The expanded reference field (Gaussian beam) is coupled into the beam path by a 50/50 beam splitter (BS), interfering with E under an angle, which enables recording the required interference pattern.

Note that this static experimental setting would also allow for implementing a physical decoding system, using a hologram, displayed by a physical component as a SLM, and a Fourier lens. With some effort and patience, supported by the digital control of the SLM, the decoding system could be adjusted appropriately, such that hologram and singularities match approximately. This would allow extracting an OAM spectrum, which might be acceptable depending on the required precision. Further, even though an SLM would allow for implementing additional corrections, these corrections would have to be determined beforehand. Hence, additional measurement steps would be required prior to OAM decoding. Additionally, the overall physical decoding approach would also be more time-consuming as each hologram (or spatially multiplexed holograms) needs to be displayed on the SLM while OAM contributions ρ_ℓ^2 have to be extracted from the camera image. Compared to this procedure, the all-digital approach is clearly advantageous. By a single interference measurement, the physical field of interest is transformed into a digital one and all required corrections can be determined and subsequently applied, such that the continuous OAM spectrum can be decoded with very high precision. We exemplify this procedure below.

Following the approach described in Figs. 3(a)–3(c), we obtain the transverse amplitude E_0 and phase ϕ distribution [see Figs. 7(b) and 7(c)] from the Fourier transform of the interference pattern, using DHPM. We observe an asymmetric distribution in intensity, partially affected by the nonideal performance of the q-plate. The phase structure shows a spiral-like distribution, revealing the embedded phase vortex with its singularity plus the wave front curvature of E at the selected z-position (=behind the ball lens focus). The singularity is approximately centered in the respective spiral of equal phase values in ϕ. Note also that DHPM can add curvatures in ϕ; however, by choosing a reference field of significantly larger beam waist, this effect is minimized.

First, we extract the OAM spectrum without considering any correction ϕ_{corr}. For this purpose, the measured E (cropped by a binary 2D mask) is digitally multiplied by the decoding holograms u_ℓ^*, which are positioned according to the embedded phase singularity found by zero-lines, and Fourier transformed afterward. Examples of the corresponding outcome intensity distributions are depicted in Fig. 7(e). Reading out the on-axis intensity values $\rho_\ell^2(0,0)$ for $\ell = [-3, 3] \in \mathbb{R}$, we obtain the normalized OAM spectrum in Fig. 7(g), blue curve. Overall, the OAM spectrum is not very clear and does not show the expected maximum at $\ell = 1$, but it is close to $\ell = 0$ with additional contributions of multiple different $\ell \in \mathbb{R}$ values. This can already be expected when taking a look at the Fourier transformed fields shown in Fig. 7(e), revealing only slight deviation from one another.

This perturbed outcome is related to the complex, asymmetric amplitude E_0 structure in combination with additional phase contributions in ϕ (wave front curvature; phase ramp). To first consider phase ramps in E, we extract $\vec{k}_E$ from the Fourier transformed interference pattern. Here, $\vec{k}_E$ is approximately equal to $\vec{k}_{ref}$ of our calibrated experimental system, resulting in a negligible phase ramp correction. When interpreting Fourier transform as focusing by a lens, the additional approximately spherical wave front curvature visible in ϕ causes a discrepancy between the plane in which OAM is correctly decoded and the actual plane of observation in Fig. 7(e). To overcome this problem, we apply a spherical phase correction (ϕ_{corr}) to the experimentally measured complex field, multiplying it by the term $\exp(-\mathrm{i}(\frac{r}{\sigma})^2)$, $\sigma = 40$, centered around the singularity. This correction term matches the wave front curvature for a Gaussian envelope of the light field E at the selected z-position. Note that a similar phase correction can be determined by a 3D ellipsoidal fit of the unwrapped measured phase, as explained in Sec. III. The corrected phase $\phi + \phi_{corr}$ is shown in Fig. 7(d). For decoding $E_0 \cdot \exp(\mathrm{i}(\phi + \phi_{corr}))$, examples of the respective intensity distributions in Fourier space are depicted in Fig. 7(f). In this case, we already observe a Gaussian-like distribution for $\ell = 1$, indicating the correct decoding of the light field. The corresponding OAM spectrum is shown in Fig. 7(g), orange curve, showing a clear maximum at $\ell = 1$. The results are in very good agreement with the simulated distributions, discussed above, proving the significant benefit of implementing the proposed single-shot, all-digital approach for OAM spectrum analysis.

VI. CONCLUSION AND DISCUSSION

To overcome typical challenges in physical experimental decoding systems, we propose a single-shot, all-digital approach for OAM spectrum analysis of complex light fields, particularly advantageous for disturbed and/or dynamically changing, high-speed systems. The approach extracts the continuous OAM spectrum with high precision due to optimized and automated identification of the decoding position and digital correction of disturbances, even dynamically changing ones. The versatile approach is based on digital holographic phase metrology (DHPM) of the light field E of interest combined with digital post-processing of the received data, also including tools of singular optics. We exemplified the procedure as well as its advantages by investigating a Laguerre–Gaussian light field ($LG_{0,1}$) passing through a ball or spheroid glass lens. In addition to numerical investigations, we provided experimental proof by determining the correct OAM spectrum of an $LG_{0,1}$ field refracted by a ball lens, applying the enabled optimization steps within our single-shot, all-digital approach.

A clear benefit of the proposed approach for OAM spectrum analysis is the option to include optimization/correction steps prior to digital spectrum decoding. As shown, the simple adjustment of the hologram position to the optical singularity/singularities, identified automatically as zero-line intersection(s), is highly effective in improving the spectrum results. Moreover, this approach enables the correction of phase factors originating from standard experimental measurement systems and procedures. In particular, the angular misalignment of observation plane and light field propagation, or the incorrect selection of the read-out position in Fourier

space ($\rho_\ell^2(k_x, k_y)$), is a commonly occurring error in experimental decoding systems. By the combination of DHPM and all-digital decoding of OAM spectrum, this error can be revealed, avoided, and/or corrected. Additionally, phase front curvatures falsifying the OAM spectrum can be detected and neutralized. Both angular mismatch and disturbing wave front curvatures can be identified automatically in the digital electric field, for instance, by applying the phase unwrapping algorithm and subsequent 3D fitting for elliptical wavefront corrections. Note that these phase corrections can also be considered as identifying an appropriate, advanced decoding hologram for a complex light field, such that the main content of the remaining field $[E \cdot \exp(\mathrm{i}\phi_{\mathrm{corr}})]$ is dominated by the OAM of light. Consequently, researchers should obviously only correct for factors that, to the best of their knowledge, do not affect the OAM of light.

The proposed approach only requires a single-shot measurement of two interfering fields. Because of this feature, it is perfectly suited for analyzing the OAM spectrum in dynamic, even high-speed, systems, with its temporal resolution only being limited by the frame rate of the implemented detector. Note, however, that in some applications, an instant, optical answer to decoding holograms might be desired, e.g., in all-optical computing. In this case, a mode sorter[63–66] might be the tool of choice, in particular when the measured OAM light fields are relatively clear (undisturbed) or deviations of the OAM spectrum are acceptable. For an optimized spectrum and in case of stronger, dynamic perturbations in the experimental system, the all-digital approach might be preferred. Improving corrections ϕ_{corr} can be adapted dynamically per shot as required by the current state of the system. This feature of our approach allows for the advanced investigation of high-speed changes in, for instance, complex fluidic flow systems, using nano-scatterers as tracer particles and OAM-carrying light fields as sensing beams.[4,57,67] Moreover, the single-shot measurement of interference patterns and its all-digital post-processing also enable the detection of small changes in the OAM spectrum, in particular, the continuous spectrum, including not only integer but also non-integer ℓ values.

SUPPLEMENTARY MATERIAL

See the supplementary material, Fig. 1, for an example of the all-digital OAM spectrum analysis in the case of multiple combined Laguerre–Gaussian beams ($\mathrm{LG}_{0,0} + \mathrm{LG}_{0,3}$).

ACKNOWLEDGMENTS

E.O., V.B., and C.D. acknowledge partial support by the German Research Foundation (DFG), under Project No. DE-486/23-1, and by the European Union (EU) Horizon 2020 program, in the Framework of the European Training Network ColOpt ITN 721465. E.O. additionally acknowledges support by the Federal Ministry of Education and Research (Bundesministerium für Bildung und Forschung, BMBF), Germany, under the DAAD PRIME program and by the Geballe Laboratory for Advanced Materials, Stanford University, USA.

AUTHOR DECLARATIONS

Conflict of Interest

The authors have no conflicts to disclose.

Author Contributions

E. Otte: Conceptualization (equal); Formal analysis (supporting); Funding acquisition (equal); Investigation (supporting); Methodology (equal); Project administration (equal); Software (supporting); Visualization (equal); Writing – original draft (lead). **V. Bobkova:** Conceptualization (equal); Formal analysis (equal); Investigation (equal); Methodology (equal); Software (supporting); Visualization (equal); Writing – original draft (equal). **S. Trinschek:** Conceptualization (equal); Formal analysis (equal); Investigation (equal); Methodology (equal); Software (lead); Visualization (equal); Writing – original draft (equal). **C. Rosales-Guzmán:** Conceptualization (supporting); Formal analysis (supporting); Investigation (supporting); Methodology (supporting); Writing – original draft (equal). **C. Denz:** Conceptualization (supporting); Funding acquisition (lead); Project administration (equal); Resources (lead); Supervision (lead); Validation (supporting); Writing – original draft (supporting); Writing – review & editing (equal).

DATA AVAILABILITY

The data that support the findings of this study are available from the corresponding author upon reasonable request.

REFERENCES

[1] L. Allen, M. W. Beijersbergen, R. J. C. Spreeuw, and J. P. Woerdman, "Orbital angular momentum of light and the transformation of Laguerre-Gaussian laser modes," Phys. Rev. A **45**, 8185–8189 (1992).
[2] M. J. Padgett, "Orbital angular momentum 25 years on (invited)," Opt. Express **25**, 11265–11274 (2017).
[3] C. Rosales-Guzmán, N. Hermosa, A. Belmonte, and J. P. Torres, "Experimental detection of transverse particle movement with structured light," Sci. Rep. **3**, 2815 (2013).
[4] A. Belmonte, C. Rosales-Guzmán, and J. P. Torres, "Measurement of flow vorticity with helical beams of light," Optica **2**, 1002–1005 (2015).
[5] M. P. J. Lavery, F. C. Speirits, S. M. Barnett, and M. J. Padgett, "Detection of spinning object using light's orbital angular momentum," Science **341**, 537–540 (2013).
[6] Y. Yang, Y. Ren, M. Chen, Y. Arita, and C. Rosales-Guzmán, "Optical trapping with structured light: A review," Adv. Photonics **3**, 034001 (2021).
[7] E. Otte and C. Denz, "Optical trapping gets structure: Structured light for advanced optical manipulation," Appl. Phys. Rev. **7**, 041308 (2020).
[8] S. W. Hell, "Far-field optical nanoscopy," Science **316**, 1153–1158 (2007).
[9] A. E. Willner, H. Huang, Y. Yan, Y. Ren, N. Ahmed, G. Xie, C. Bao, L. Li, Y. Cao, Z. Zhao, J. Wang, M. P. J. Lavery, M. Tur, S. Ramachandran, A. F. Molisch, N. Ashrafi, and S. Ashrafi, "Optical communications using orbital angular momentum beams," Adv. Opt. Photonics **7**, 66 (2015).
[10] A. E. Willner, Z. Zhao, C. Liu, R. Zhang, H. Song, K. Pang, K. Manukyan, H. Song, X. Su, G. Xie, Y. Ren, Y. Yan, M. Tur, A. F. Molisch, R. W. Boyd, H. Zhou, N. Hu, A. Minoofar, and H. Huang, "Perspectives on advances in high-capacity, free-space communications using multiplexing of orbital-angular-momentum beams," APL Photonics **6**, 030901 (2021).
[11] D. McArthur, A. M. Yao, and F. Papoff, "Scattering of light with angular momentum from an array of particles," Phys. Rev. Res. **2**, 013100 (2020).
[12] M. S. Soskin, V. N. Gorshkov, M. V. Vasnetsov, J. T. Malos, and N. R. Heckenberg, "Topological charge and angular momentum of light beams carrying optical vortices," Phys. Rev. A **56**, 4064–4075 (1997).
[13] M. V. Vasnetsov, J. P. Torres, D. V. Petrov, and L. Torner, "Observation of the orbital angular momentum spectrum of a light beam," Opt. Lett. **28**, 2285–2287 (2003).

[14]O. Bryngdahl, "Radial- and circular-fringe interferograms," J. Opt. Soc. Am. **63**, 1098–1104 (1973).
[15]J. Leach, M. J. Padgett, S. M. Barnett, S. Franke-Arnold, and J. Courtial, "Measuring the orbital angular momentum of a single photon," Phys. Rev. Lett. **88**, 257901 (2002).
[16]H. Wei and X. Xue, "Simplified measurement of the orbital angular momentum of single photons," Opt. Commun. **223**, 117–122 (2003).
[17]J. Leach, J. Courtial, K. Skeldon, S. M. Barnett, S. Franke-Arnold, and M. J. Padgett, "Interferometric methods to measure orbital and spin, or the total angular momentum of a single photon," Phys. Rev. Lett. **92**, 013601 (2004).
[18]S. Li, P. Zhao, X. Feng, K. Cui, F. Liu, W. Zhang, and Y. Huang, "Measuring the orbital angular momentum spectrum with a single point detector," Opt. Lett. **43**, 4607–4610 (2018).
[19]G. Kulkarni, R. Sahu, O. S. Magaña-Loaiza, R. W. Boyd, and A. K. Jha, "Single-shot measurement of the orbital-angular-momentum spectrum of light," Nat. Commun. **8**, 1054 (2017).
[20]R. Aboushelbaya, K. Glize, A. F. Savin, M. Mayr, B. Spiers, R. Wang, N. Bourgeois, C. Spindloe, R. Bingham, and P. A. Norreys, "Measuring the orbital angular momentum of high-power laser pulses," Phys. Plasmas **27**, 053107 (2020).
[21]C.-S. Guo, L.-L. Lu, and H.-T. Wang, "Characterizing topological charge of optical vortices by using an annular aperture," Opt. Lett. **34**, 3686–3688 (2009).
[22]Y. Han and G. Zhao, "Measuring the topological charge of optical vortices with an axicon," Opt. Lett. **36**, 2017–2019 (2011).
[23]J. M. Hickmann, E. J. S. Fonseca, W. C. Soares, and S. Chávez-Cerda, "Unveiling a truncated optical lattice associated with a triangular aperture using light's orbital angular momentum," Phys. Rev. Lett. **105**, 053904 (2010).
[24]M. Mazilu, A. Mourka, T. Vettenburg, E. M. Wright, and K. Dholakia, "Simultaneous determination of the constituent azimuthal and radial mode indices for light fields possessing orbital angular momentum," Appl. Phys. Lett. **100**, 231115 (2012).
[25]C.-S. Guo, X. Cheng, X.-Y. Ren, J.-P. Ding, and H.-T. Wang, "Optical vortex phase-shifting digital holography," Opt. Express **12**, 5166–5171 (2004).
[26]J. Zhu, P. Zhang, Q. Li, F. Wang, C. Wang, Y. Zhou, J. Wang, H. Gao, L. C. Kwek, and F. Li, "Measuring the topological charge of orbital angular momentum beams by utilizing weak measurement principle," Sci. Rep. **9**, 7993 (2019).
[27]H.-L. Zhou, D.-Z. Fu, J.-J. Dong, P. Zhang, D.-X. Chen, X.-L. Cai, F.-L. Li, and X.-L. Zhang, "Orbital angular momentum complex spectrum analyzer for vortex light based on the rotational Doppler effect," Light: Sci. Appl. **6**, e16251 (2017).
[28]M. P. J. Lavery, D. J. Robertson, G. C. G. Berkhout, G. D. Love, M. J. Padgett, and J. Courtial, "Refractive elements for the measurement of the orbital angular momentum of a single photon," Opt. Express **20**, 2110–2115 (2012).
[29]N. K. Fontaine, R. Ryf, H. Chen, D. T. Neilson, K. Kim, and J. Carpenter, "Laguerre-Gaussian mode sorter," Nat. Commun. **10**, 1865 (2019).
[30]J. Wang, S. Chen, and J. Liu, "Orbital angular momentum communications based on standard multi-mode fiber (invited paper)," APL Photonics **6**, 060804 (2021).
[31]A. Trichili, M. A. Cox, B. S. Ooi, and M.-S. Alouini, "Roadmap to free space optics," J. Opt. Soc. Am. B **37**, A184–A201 (2020).
[32]A. Forbes, A. Dudley, and M. McLaren, "Creation and detection of optical modes with spatial light modulators," Adv. Opt. Photonics **8**, 200–227 (2016).
[33]M. V. Vasnetsov, V. A. Pas'ko, and M. S. Soskin, "Analysis of orbital angular momentum of a misaligned optical beam," New J. Phys. **7**, 46 (2005).
[34]M. A. Cox, L. Maqondo, R. Kara, G. Milione, L. Cheng, and A. Forbes, "The resilience of Hermite– and Laguerre–Gaussian modes in turbulence," J. Lightwave Technol. **37**, 3911–3917 (2019).
[35]Y.-D. Liu, C. Gao, X. Qi, and H. Weber, "Orbital angular momentum (OAM) spectrum correction in free space optical communication," Opt. Express **16**, 7091–7101 (2008).
[36]J. Lin, X.-C. Yuan, M. Chen, and J. C. Dainty, "Application of orbital angular momentum to simultaneous determination of tilt and lateral displacement of a misaligned laser beam," J. Opt. Soc. Am. A **27**, 2337–2343 (2010).
[37]S. Lohani and R. T. Glasser, "Turbulence correction with artificial neural networks," Opt. Lett. **43**, 2611–2614 (2018).
[38]Q. Zhao, S. Hao, Y. Wang, L. Wang, X. Wan, and C. Xu, "Mode detection of misaligned orbital angular momentum beams based on convolutional neural network," Appl. Opt. **57**, 10152–10158 (2018).
[39]P. Zhao, S. Li, Y. Wang, X. Feng, C. Kaiyu, L. Fang, W. Zhang, and Y. Huang, "Identifying the tilt angle and correcting the orbital angular momentum spectrum dispersion of misaligned light beam," Sci. Rep. **7**, 7873 (2017).
[40]J. R. Fienup, "Reconstruction of an object from the modulus of its Fourier transform," Opt. Lett. **3**, 27–29 (1978).
[41]E. Otte, K. Tekce, and C. Denz, "Spatial multiplexing for tailored fully-structured light," J. Opt. **20**, 105606 (2018).
[42]C. Rosales-Guzmán, N. Bhebhe, N. Mahonisi, and A. Forbes, "Multiplexing 200 spatial modes with a single hologram," J. Opt. **19**, 113501 (2017).
[43]S. Li and J. Wang, "Simultaneous demultiplexing and steering of multiple orbital angular momentum modes," Sci. Rep. **5**, 15406 (2015).
[44]A. E. Siegman, *Lasers* (University Science Books, Mill Valley, 1986).
[45]G. D. Boyd and J. P. Gordon, "Confocal multimode resonator for millimeter through optical wavelength masers," Bell Syst. Tech. J. **40**, 489–508 (1961).
[46]B. E. Saleh and M. C. Teich, *Fundamentals of Photonics* (John Wiley & Sons, Hoboken, 2019).
[47]A. Schutza, "Transmission of quantum information via Laguerre-Gaussian modes," McNair Scholars J. **14**(1), 8 (2010).
[48]M. R. Dennis, K. O'Holleran, and M. J. Padgett, in *Singular Optics: Optical Vortices and Polarization Singularities* (Elsevier, 2009), Chap. 5, pp. 293–363.
[49]M. S. Soskin and M. V. Vasnetsov, in *Singular Optics* (Elsevier, 2001), Chap. 4, pp. 219–277.
[50]G. Gibson, J. Courtial, M. J. Padgett, M. Vasnetsov, V. Pas'ko, S. M. Barnett, and S. Franke-Arnold, "Free-space information transfer using light beams carrying orbital angular momentum," Opt. Express **12**, 5448–5456 (2004).
[51]M. Mirhosseini, O. S. Magaña-Loaiza, M. N. O'Sullivan, B. Rodenburg, M. Malik, M. P. J. Lavery, M. J. Padgett, D. J. Gauthier, and R. W. Boyd, "High-dimensional quantum cryptography with twisted light," New J. Phys. **17**, 033033 (2015).
[52]M. Takeda, H. Ina, and S. Kobayashi, "Fourier-transform method of fringe-pattern analysis for computer-based topography and interferometry," J. Opt. Soc. Am. **72**, 156–160 (1982).
[53]A. Zannotti, "Realization and exploration of structured light and photonic structures," in *Caustic Light in Nonlinear Photonic Media* (Springer, Cham, 2020), Chap. 2, pp. 31–49.
[54]M. R. Dennis, "Topological singularities in wave fields," Ph.D. thesis, University of Bristol, 2001.
[55]E. Otte, *Structured Singular Light Fields* (Springer Nature, Cham, 2021).
[56]E. Otte and C. Denz, "Customization and analysis of structured singular light fields," J. Opt. **23**, 073501 (2021).
[57]V. Bobkova, S. Trinschek, E. Otte, and C. Denz, "Analyzing light-structuring features of droplet lenses on liquid-repelling surfaces," Opt. Express **30**, 5937–5952 (2022).
[58]B. Andreas, G. Mana, and C. Palmisano, "Vectorial ray-based diffraction integral," J. Opt. Soc. Am. A **32**, 1403–1424 (2015).
[59]B. Andreas, G. Mana, and C. Palmisano, "Vectorial ray-based diffraction integral: Erratum," J. Opt. Soc. Am. A **33**, 559–560 (2016).
[60]Z. Zhao, H. Zhang, Z. Xiao, H. Du, Y. Zhuang, C. Fan, and H. Zhao, "Robust 2D phase unwrapping algorithm based on the transport of intensity equation," Meas. Sci. Technol. **30**, 015201 (2018).
[61]L. Marrucci, C. Manzo, and D. Paparo, "Optical spin-to-orbital angular momentum conversion in inhomogeneous anisotropic media," Phys. Rev. Lett. **96**, 163905 (2006).
[62]E. Karimi, G. Zito, B. Piccirillo, L. Marrucci, and E. Santamato, "Hypergeometric-Gaussian modes," Opt. Lett. **32**, 3053–3055 (2007).
[63]G. C. G. Berkhout, M. P. J. Lavery, J. Courtial, M. W. Beijersbergen, and M. J. Padgett, "Efficient sorting of orbital angular momentum states of light," Phys. Rev. Lett. **105**, 153601 (2010).

[64]G. Ruffato, M. Massari, and F. Romanato, "Compact sorting of optical vortices by means of diffractive transformation optics," Opt. Lett. **42**, 551–554 (2017).
[65]G. Ruffato, M. Girardi, M. Massari, E. Mafakheri, B. Sephton, P. Capaldo, A. Forbes, and F. Romanato, "A compact diffractive sorter for high-resolution demultiplexing of orbital angular momentum beams," Sci. Rep. **8**, 10248 (2018).
[66]C. Wan, J. Chen, and Q. Zhan, "Compact and high-resolution optical orbital angular momentum sorter," APL Photonics **2**, 031302 (2017).
[67]A. Ryabtsev, S. Pouya, A. Safaripour, M. Koochesfahani, and M. Dantus, "Fluid flow vorticity measurement using laser beams with orbital angular momentum," Opt. Express **24**, 11762–11767 (2016).